ROYAL SOCIETY
OF CHEMISTRY

Check for updates

Structural design strategies for superionic sodium halide solid electrolytes†

Seungho Yu, [ID] *[ab] Kwangnam Kim, [ID] [c] Brandon C. Wood,[c] Hun-Gi Jung [ID] [ab] and Kyung Yoon Chung [ID] [ab]

Sodium all-solid-state batteries (ASSBs) with superionic solid electrolytes (SEs) show substantial potential for large-scale energy-storage applications. Recently, lithium halide SEs have attracted attention owing to their potential compatibility with high-voltage cathode materials and high ionic conductivity. Although sodium halide SEs are believed to exhibit good electrochemical stability, very few compounds have been reported. This study provides design principles for superionic sodium halide SEs through systematic theoretical investigations of Na_3MX_6 (X = Cl, Br, and I). The Na_3MX_6 structures depend on the types and sizes of M and X: Na_3MCl_6 and Na_3MBr_6 prefer the $P\bar{3}1c$, $P2_1/n$ and $R\bar{3}$ phases, whereas Na_3MI_6 prefers the $C2/m$ phase. The Na_3MI_6 $C2/m$ phase is found to exhibit reasonably high ionic conductivity ($\sim10^{-4}$ S cm^{-1}) and anion mixing with Br further improve Na-ion migration, leading to an even higher ionic conductivity ($\sim10^{-3}$ S cm^{-1}) for $Na_3MBr_3I_3$. The material design principles in this study provide fundamental guidelines for the development of superionic Na halide SEs for high-voltage Na ASSBs.

Introduction

The development of next-generation batteries with high energy density and enhanced safety is required for emerging applications, such as energy storage systems (ESS) and electric vehicles.[1] All-solid-state batteries (ASSBs) with solid electrolytes (SEs) are promising candidates for next-generation batteries.[2,3] ASSBs resolve the safety concerns of conventional Li-ion batteries by replacing flammable liquid electrolytes with nonflammable inorganic SEs.[4] ASSBs with SEs also enable the use of metallic anodes that exhibit significantly higher energy densities than conventional anode materials.[5] Recently, various types of post-Li batteries with new cations such as Na, K, and Mg have been investigated owing to their low cost and high energy density.[6–11] Among the post-Li batteries, Na-ion batteries have attracted increasing attention because of the abundance of Na.[12,13] Na ASSBs have been investigated for large-scale applications, such as ESS, which require high safety.[14,15]

Sulfide SEs have been widely studied for applications in Na ASSBs owing to their high ionic conductivity of 1–10 mS cm^{-1} for Na_3PS_4, Na_3SbS_4 and $Na_{11}Sn_2PS_{12}$.[16–20] However, sulfide SEs

are generally unstable in moisture and exhibit a narrow electrochemical stability window.[21,22] Oxide SEs (NASICONs and β-alumina) are chemically stable and can exhibit a high ionic conductivity of ~1 mS cm^{-1}, but require a high-temperature sintering process to resolve the interfacial resistance.[23,24] Recently, halide SEs have been reported as promising SEs owing to their wide electrochemical stability window and compatibility with high-voltage cathode materials.[25–28] Li ternary chlorides, Li_3MCl_6, exhibit good chemical stability against high-voltage cathode materials (~4 V) and have high ionic conductivity of 0.5–3 mS cm^{-1} for Li_3YCl_6, Li_3InCl_6 and Li_3ScCl_6.[29–32]

Although Na halides are expected to exhibit wide electrochemical stability,[33] very few Na halide SEs, such as Na_3YCl_6, Na_3ErCl_6, Na_2ZrCl_6 and Zr-substituted $Na_{3-x}M_{1-x}Zr_xCl_6$ (M = Y and Er)—all of which have low ionic conductivity below 10^{-4} S cm^{-1}—have been reported.[34–36] Owing to the ionic radius of Na (102 pm), being larger than that of Li (76 pm), Na_3MCl_6 exhibited different crystal structures of $P\bar{3}1c$, $P2_1/n$ and $R\bar{3}$ with lower ionic conductivity than the crystal structures of Li_3MCl_6, such as $C2/m$ and $P\bar{3}m1$.[37] Theoretical studies predicted the phase-dependent ionic conductivities of Na_3YBr_6 and Na_3YI_6,[38,39] but only a few studies have reported on the phases of Na bromides and iodides, Na_3MX_6 (X = Br and I).[40] This study aims to provide guidelines for the design of novel Na halide SEs, Na_3MX_6 (X = Cl, Br and I), through systematic investigations of their structural preference, phase stability, electrochemical stability and transport properties.

This study shows that the structures of Na_3MX_6 are strongly dependent on the types and sizes of M and X. In particular, Na_3MX_6 generally exhibited $P\bar{3}1c$, $P2_1/n$, $R\bar{3}$ and $C2/m$ phases,

[a]Energy Storage Research Center, Korea Institute of Science and Technology, 5, Hwarang-ro 14-gil, Seongbuk-gu, Seoul 02792, Republic of Korea. E-mail: shyu@kist.re.kr

[b]Division of Energy & Environment Technology, KIST School, Korea University of Science and Technology, Seoul 02792, Republic of Korea

[c]Materials Science Division, Lawrence Livermore National Laboratory, 94550, Livermore, USA

† Electronic supplementary information (ESI) available. See DOI: https://doi.org/10.1039/d2ta05158c

This journal is © The Royal Society of Chemistry 2022

J. Mater. Chem. A, 2022, **10**, 24301–24309 | 24301

while Na_3MX_6 with relatively small M cations preferred the $NaMX_4$ ($P2_12_12_1$) phase.[41,42] Na_3MCl_6 and Na_3MBr_6 preferred the $P\bar{3}1c$, $P2_1/n$ and $R\bar{3}$ phases, with the phase transitions depending on the radius of M. Na_3MI_6 preferred the $C2/m$ phase and showed a high ionic conductivity ($\sim10^{-4}$ S cm^{-1}). Anion mixing with Br in Na_3MI_6 further improved Na-ion migration, exhibiting a high ionic conductivity ($\sim10^{-3}$ S cm^{-1}) that is two orders of magnitude higher than the value reported for competing Na halide SEs. The material design principles in this study offer substantial promise for the development of practical superionic Na halide SEs.

Methods

First principles calculations were performed based on the density functional theory (DFT) with a plane-wave basis set, as implemented in the Vienna *Ab initio* Simulation Package (VASP).[43,44] The projector augmented wave method (PAW) was used for the core and valence electron interactions[45] and the generalized gradient approximation (GGA) of Perdew–Burke–Ernzerhof (PBE) was employed for the exchange–correlation energy functional.[46] A van der Waals (vdW) density functional (optB86b-vdW) was used to address vdW interactions in layered Na halide structures.[47] An energy cutoff of 520 eV was used for the plane-wave basis sets and the *k*-point mesh was determined using the Python Materials Genomics (pymatgen) package,[48] including a *k*-point density of at least 1000 per atom. Ionic relaxations were performed until the forces were less than 0.01 eV Å^{-1}, with a convergence criterion of 10^{-5} eV for the electronic self-consistency loop.

The simulation cells of sodium halides Na_3MX_6 (X = Cl, Br and I) were generated based on the experimental structures of Na_3MX_6 that exhibited trigonal $P\bar{3}1c$ (#163),[49,50] monoclinic $P2_1/n$ (#14),[34,35] trigonal $R\bar{3}$ (#148)[51] and monoclinic $C2/m$ (#12)[29] crystal structures. The trigonal $P\bar{3}m1$ (#164) Li chloride structure, Li_3MX_6,[27] was also used to prepare Na_3MX_6 simulation cells. Among the possible ionic configurations for the partially occupied sites in the $R\bar{3}$, $P2_1/n$ and $P\bar{3}m1$ phases, the Na_3MX_6 structure with the lowest total energy was used for subsequent calculations. Details of the structural information of $C2/m$ and $P\bar{3}m1$ phases are provided in Table S1.† Various metal elements in +3 oxidation states have been considered for ternary metal halides, Na_3MX_6, including group 3 elements (Sc, Lu and Y), group 13 elements (Al, Ga, In and Tl), group 15 elements (Bi) and lanthanides (Yb, Tm, Er, Ho, Dy, Tb, Gd, Sm, Nd and La). The transition metals with multiple oxidation states were excluded in this study. The phase stability of Na_3MX_6 (X = Cl, Br and I) was evaluated by calculating the decomposition energy, E_d, against the competing stable phases NaX and MX_3. The metastable Na_3MX_6 phase with an E_d below 25 meV per atom was considered to be a stable phase, owing to stabilization by entropic effects and kinetic inhibition. Further experimental studies can be performed to identify the stable structure of Na_3MX_6, based on the theoretical works.

The Na-ion potential energy landscape in Na_3MX_6 was obtained using the bond-valence site energy (BVSE) method, as implemented in SoftBV software.[52] The potential energy of the

Na sites was calculated using the Morse-type interaction potential with a grid density of 0.1 Å. The Na-ion migration path was predicted using the isosurface of the Na-ion probability density and the minimum energy value between the migration paths for the Na-ion migration energy barrier was obtained. Na-ion diffusivity in Na_3MX_6 was examined using *ab initio* molecular dynamics (AIMD) simulations with an energy cutoff of 350 eV, Γ-point-only *k*-point grid and the NVT ensemble with a Nosé–Hoover thermostat. A $2 \times 2 \times 1$ supercell was used for $P\bar{3}1c$, $P2_1/n$ and $R\bar{3}$, and a $2 \times 1 \times 2$ supercell was used for the $C2/m$ structure for the AIMD calculations corresponding to 80 atoms for the $P\bar{3}31c$, $P2_1/n$ and $C2/m$, and 120 atoms for $R\bar{3}$ structures. The Na-ion diffusivity was evaluated using the mean squared displacement (MSD) at five different temperatures (700, 750, 800, 900 and 1000 K) for a window of 100 to 200 ps, with a time step of 2 fs. Data from the AIMD simulations were analyzed using the diffusion analysis module of the pymatgen package.[48] The total mean squared displacement (TMSD) and effective ion jumps were calculated to evaluate the relative standard deviation of diffusivity based on previous studies.[53,54] The diffusion coefficient, D, was derived using the TMSD of Na ions as a function of the time interval, Δt:

$$D = \frac{1}{2d\Delta t}\frac{\mathrm{TMSD}(\Delta t)}{n} = \frac{1}{2d\Delta tn}\sum_{i=1}^{n}\frac{1}{N_{\Delta t}}\sum_{t=0}^{t_{tot}-\Delta t}|r_i(t+\Delta t)-r_i(t)|^2 \tag{1}$$

where d is the dimensionality, n is the total number of Na ions, $N_{\Delta t}$ is the total number of time intervals and r_i is the Na ion trajectory. The ionic conductivity, σ, was calculated using the Nernst–Einstein equation:

$$\sigma = \frac{(ze)^2cD}{k_BT} \tag{2}$$

where z is the valence of the ion, e is the elementary charge, c is the concentration of the ion, D is the diffusion coefficient, k_B is the Boltzmann constant and T is the temperature. Na-ion migration trajectories during the AIMD simulations were observed using a $25 \times 25 \times 25$ grid mesh. Isosurfaces of the ionic probability densities were obtained to visualize ion migration using the mean ionic probability density (P_0).

The electrochemical stability of Na_3MX_6 (X = Cl, Br and I) was investigated using the Materials Project (MP) database.[55] The grand potential phase diagram as a function of the chemical potential of Na was obtained using the pymatgen package[48] to evaluate the electrochemical stability window of Na_3MX_6. The total energies of Na_3MX_6 were updated using equivalent settings in the MP for the calculations. The oxidation and reduction potentials with their phase equilibria were examined to determine the electrochemical stability of Na_3MX_6. Na_3MX_6 compounds that were unstable against phase decomposition were excluded from the electrochemical stability calculations.

Results

The most stable structure of Na_3MX_6 (X = Cl, Br and I) among trigonal $P\bar{3}1c$, monoclinic $P2_1/n$, trigonal $R\bar{3}$, monoclinic $C2/m$

24302 | *J. Mater. Chem. A*, 2022, **10**, 24301–24309

This journal is © The Royal Society of Chemistry 2022

and trigonal $P\bar{3}m1$ was determined by comparing the total energies of the phases, as shown in Fig. S1–S3 and Table S2.† Although the energy differences among the phases are small and several phases can be considered as the most stable phase, there exists a general trend for phase transitions among the structures, as a function of the size of cation (M) and anion (X). The phase preference for Na_3MCl_6 agrees with a previous work[37] showing that Na_3MCl_6 with relatively small M cations prefers the trigonal $P\bar{3}1c$ phase, whereas Na_3MCl_6 with modestly large M cations prefers the monoclinic $P2_1/n$ phase and Na_3MCl_6 with even larger M cations above 90 pm prefers the $R\bar{3}$ phase, as shown in Fig. S1.† The phase preference of Na_3MBr_6 was found to be comparable to that of Na_3MCl_6 in the $P\bar{3}1c$, $P2_1/n$ and $R\bar{3}$ phases; however, the driving force for the phase transitions to $P2_1/n$ and $R\bar{3}$ for Na_3MBr_6 was relatively weaker than for Na_3MCl_6, as shown in Fig. S1.† Therefore, phase transitions (from $P\bar{3}1c$ to $P2_1/n$ and from $P2_1/n$ to $R\bar{3}$) require relatively larger M cations in Na_3MBr_6 compared with Na_3MCl_6. Na_3MCl_6 and Na_3MBr_6 preferred $P\bar{3}1c$, $P2_1/n$ and $R\bar{3}$ phases, while Na_3MI_6 preferentially exhibited the $C2/m$ phase over the other phases. The energy difference plot in Fig. S2† shows this phase preference of $C2/m$ compared with other phases for Na_3MI_6. The energy differences for the $P\bar{3}1c$, $P2_1/n$, $R\bar{3}$, $C2/m$ and $P\bar{3}m1$ phases for Na_3MX_6 (X = Cl, Br and I) are listed in Table S2.† The energy difference among the phases was negligible for Na_3MBr_6 since they were in the phase transition region. The ground state of structure with the lowest energy should be examined to obtain the accurate results.

The phase stability of Na_3MX_6 (X = Cl, Br and I) was evaluated using the decomposition energy, E_d, against the competing stable phases, NaX and MX_3. The most stable phase of MX_3 among the experimental structures listed in Tables S3 and S4† was used to evaluate E_d. The E_d values for the $P\bar{3}1c$, $P2_1/n$, $R\bar{3}$, $C2/m$ and $P\bar{3}m1$ structures are illustrated as a heat map in Fig. S3 and S4.† Na_3MX_6 phases with negative E_d values (dark blue) were considered stable against decomposition to NaX and MX_3, whereas Na_3MX_6 phases with positive E_d values under 25 meV per atom were considered metastable phases owing to the entropic effects and kinetic barrier of decomposition. Na_3MX_6 phases with positive E_d values above 25 meV per atom (light brown) were considered unstable phases, which generally included large M cations ($M_{radii} > 95$ pm), such as Sm, Nd and La. Na_3MCl_6 typically exhibit stable phases, whereas most Na_3MBr_6 and Na_3MI_6 exhibit metastable or unstable phases. The Na_3MI_6 E_d values are higher than those for Na_3MBr_6, suggesting that the relatively large X in Na_3MX_6 decreases phase stability. The most stable Na_3MX_6 phases with the lowest E_d value among the $P\bar{3}1c$, $P2_1/n$, $R\bar{3}$, $C2/m$ and $P\bar{3}m1$ phases are shown in Fig. 1(a) and Tables S5 and S6.†

The Na_3MX_6 structures are strongly dependent on the sizes of M and X. The octahedral factor, t, was employed to investigate the structural preferences of Na_3MX_6. Defined as the ratio of the radius of cation to anion (r^+/r^-), this octahedral factor between M and X ($t_{MX} = r_M/r_X$) effectively described the structure of the Li–M–X compound in an earlier study.[25,56] Li–M–X was found to form MX_8 cubes for high values of t_{MX}, such as fluorides, while the structures changed to MX_6 octahedra for

lower values of t_{MX}, such as chlorides (Li_3MCl_6). The Li–M–X compound exhibited an MX_4 tetrahedron upon further decrease in t_{MX}, forming $LiMX_4$.[25,56] The M–X structural changes in the Na–M–X compounds were consistent with these prior results for the Li–M–X compounds, suggesting that moderate values of t_{MX} result in Na_3MX_6 phases, whereas lower values of t_{MX} result in $NaMX_4$ phases. Na–M–X compounds with relatively small cations, such as Al and Ga, showed low t_{MX} values, exhibiting the $NaMX_4$ ($P2_12_12_1$) phase instead of the Na_3MX_6 phase, as shown in Table S7.†

The octahedral factor between A and X ($t_{AX} = r_A/r_X$, A = Li and Na) and t_{MX} was evaluated to investigate the structure of Na_3MX_6 in Fig. 1(b–d). Using the t_{AX} and t_{MX} as x and y values in the two-dimensional plot in Fig. 1(b), the structural preferences of A_3MX_6 among the $P\bar{3}1c$, $P2_1/n$, $R\bar{3}$, $C2/m$ and $P\bar{3}m1$ phases were assessed. Data that lie on the dashed line in Fig. 1(b) feature t_{AX} that is equivalent to t_{MX}, indicating that the sizes of octahedra of MX_6 and AX_6 are comparable (*e.g.*, Li_3ScCl_6). Data points for A_3MX_6 lie above or below this dashed line when the size of M is larger or smaller than A, respectively. Na_3MX_6 (X = Cl, Br and I) is positioned below the dashed line because the ionic radius of Na (102 pm) is typically larger than that of the M cations. Most Li chlorides and bromides, Li_3MX_6 (X = Cl and Br), were found to lie above the dashed line because of the smaller ionic radius of Li (76 pm) compared with that of the M cations. Li fluorides and iodides (Li_3MX_6, X = F and I) were disregarded in this plot because they exceeded the span of t for Na_3MX_6, exhibiting high values of t_{MX} above 0.6 for Li_3MF_6 and low values of t_{AX} under 0.35 for Li_3MI_6.

In Fig. 1(b), the $NaMX_4$ ($P2_12_12_1$) phase for relatively small M cations with low values of t_{MX} in Table S7† is represented in yellow. For Na_3MX_6 with higher values of t_{MX} than those of $NaMX_4$, the most stable structural phase among $P\bar{3}1c$, $P2_1/n$, $R\bar{3}$, $C2/m$ and $P\bar{3}m1$ is represented by black, red, blue, green and purple, respectively. Li_3MX_6 compounds (X = Cl and Br) generally exhibited the $C2/m$ phase, whereas the $P\bar{3}m1$ phase was the stable phase for Li_3MCl_6 with large M cations, corresponding to a high t_{MX} above 0.5.[57] Na_3MI_6 showed similar values of t_{AX} and t_{MX} ($t_{AX} \sim 0.45$ and $0.35 < t_{MX} < 0.5$) to Li_3MCl_6, resulting in a preference for the $C2/m$ phase. As the size of the X anion increases ($t_{AX} > 0.5$), Na_3MX_6 (X = Cl and Br) was found to prefer the $P\bar{3}1c$, $P2_1/n$ and $R\bar{3}$ phases to the $C2/m$ phase, with $P\bar{3}1c$–$P2_1/n$–$R\bar{3}$ phase transitions occurring for Na_3MX_6 (X = Cl and Br) with increased size of M (*i.e.*, with larger t_{MX}).

The phase preferences of A_3MX_6 (A = Li and Na; X = Cl, Br and I) with M in the p-block (groups 13 and 15; M = Al, Ga, In, Tl and Bi) was observed to be slightly different, with phase transitions (from $P2_12_12_1$ to $C2/m$, from $P2_12_12_1$ to $P\bar{3}1c$, from $P\bar{3}1c$ to $P2_1/n$) occurring with relatively large M cations. For example, the group 3 element Sc (75 pm) exhibited phase transitions from $P2_12_12_1$ to $P\bar{3}1c$ for Na_3ScI_6 and from $P\bar{3}1c$ to $P2_1/n$ for Na_3ScCl_6, whereas the group 13 element In, with a relatively large ionic radius (80 pm), exhibited $P2_12_12_1$ for $NaInI_4$ and $P\bar{3}1c$ for Na_3InCl_6. The difference in electronegativity between M and X is smaller for the p-block elements than for the d- and f-block elements (*i.e.*, group 3 elements and lanthanides), resulting in weaker Coulomb interactions and different phase-transition
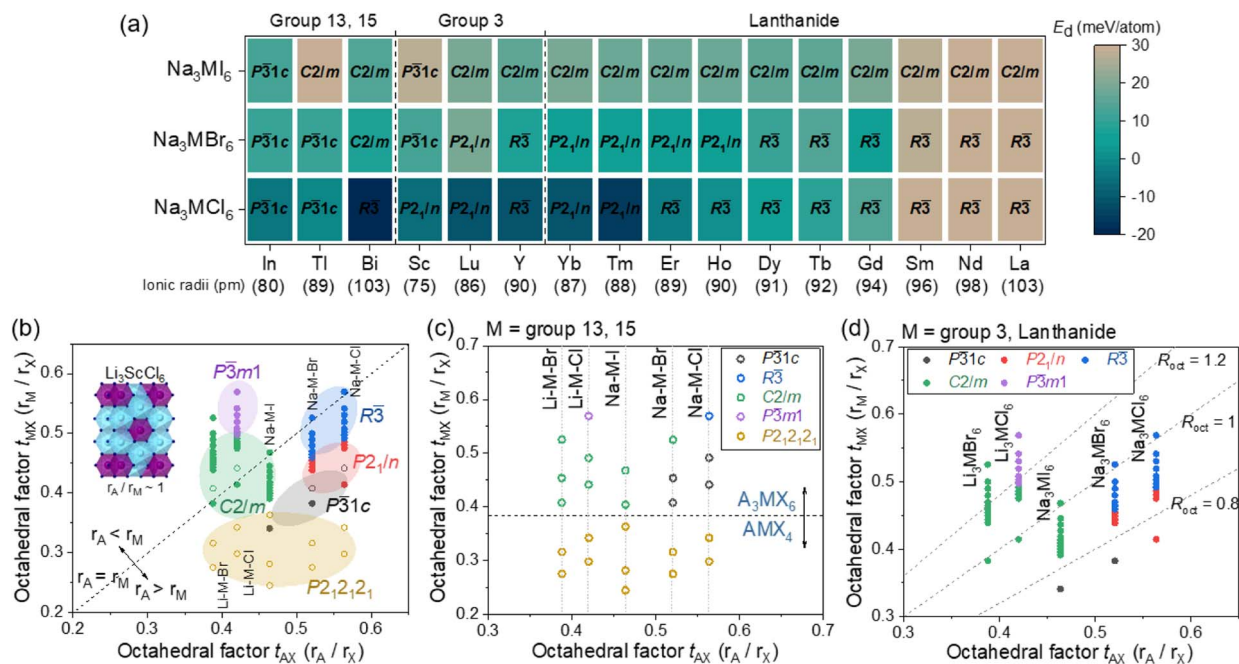
Fig. 1 (a) Heat map for the decomposition energy (E_d) of Na halides (Na_3MX_6, X = Cl, Br and I) against the competing phases NaX and MX_3. The most stable phase for the crystal structures of $P\bar{3}1c$, $P2_1/n$, $R\bar{3}$, $C2/m$ and $P\bar{3}m1$ was used to evaluate E_d for Na_3MX_6. (b–d) Structural preference tendencies of the crystal systems for $P\bar{3}1c$, $P2_1/n$, $R\bar{3}$, $C2/m$, $P\bar{3}m1$ and $P2_12_12_1$ as a function of the octahedral factors for AX_6 (r_A/r_X) and MX_6 (r_M/r_X) for Li and Na metal ternary halides based on M elements: (b) all elements, (c) group 13 and 15 elements, (d) group 3 and lanthanide elements. Compounds in same composition group (A–M–X) are aligned vertically in (b–d). R_{oct} in (d) corresponds to the ratio of r_A to r_M.

trends.[57] Hence, the phase transitions of A_3MX_6 with p-block elements occurred only with a relatively large M, for which the difference in electronegativity becomes appreciable. The data for A_3MX_6 with p-block elements are presented using open symbols in Fig. 1(b and c) and the phase preferences of A_3MX_6 in Fig. 1(b) are divided into two plots based on the M cation: Fig. 1(c) for group 13 and 15 elements and Fig. 1(d) for group 3 and lanthanide elements.

Fig. 1(c) shows the preference of the MX_4 tetrahedron for relatively small p-block elements with low values of t_{MX} (<0.38), forming the $NaMX_4$ ($P2_12_12_1$) phase. Because this $P2_12_12_1$ phase includes MX_4 tetrahedron showing low ionic conductivity,[26] M cations with small ionic radii may be neglected in the design of superionic Na–M–X SEs. The phase preference of A_3MX_6 for group 3 elements and lanthanides with relatively large ionic radii (>74 pm) is shown in Fig. 1(d). Here, the ratio of octahedral factors, $R_{oct} = t_{MX}/t_{AX} = r_M/r_A$ was used to classify the A_3MX_6 phases. The value of R_{oct} is higher or lower than 1 when the cation M is larger or smaller than A, respectively. The R_{oct} values were generally 1.0–1.3 for Li_3MCl_6 and they exhibited a phase transition from $C2/m$ to $P\bar{3}m1$ at a R_{oct} value of approximately 1.2. The R_{oct} values were generally 0.8–1.0 for Na_3MX_6 (X = Cl, Br and I) because of the large ionic radius of Na (102 pm). Na_3MI_6 maintained the $C2/m$ phase in this range, whereas Na_3MBr_6 and Na_3MCl_6 exhibited a phase transition from $P2_1/n$ to $R\bar{3}$ phase at R_{oct} values of approximately 0.85.

The Na-ion potential energy landscapes for the $P\bar{3}1c$, $P2_1/n$ and $R\bar{3}$ phases of Na_3MX_6 (Cl and Br) and the $C2/m$ phase of Na_3MI_6 were predicted using the BVSE method. The

experimental structures of Na_3InCl_6, Na_3ErCl_6, Na_3GdCl_6 and Na_3GdI_6 were used to examine Na-ion migration in the $P\bar{3}1c$, $P2_1/n$, $R\bar{3}$ and $C2/m$ phases, respectively. The isosurface of the Na-site energy (light blue) was obtained to visualize the Na-ion migration pathways, as shown in Fig. 2 and S5–S9.† The calculation results indicate that the trigonal $P\bar{3}1c$ and $R\bar{3}$ phases of Na_3MCl_6 show 1D paths between octahedral sites (Oct.–Oct.) along the z-axis as well as 3D paths between octahedral sites via tetrahedral interstitial sites (Oct.–Tet.–Oct.). The monoclinic $P2_1/n$ phase of Na_3MCl_6 exhibits 3D paths between octahedral and prism sites (Oct.–Prism) and between octahedral and prism sites via tetrahedral interstitial sites (Oct.–Tet.–Prism), agreeing with previous studies.[37] The Na-ion migration paths in Na_3InBr_6 ($P\bar{3}1c$), Na_3ErBr_6 ($P2_1/n$) and Na_3GdBr_6 ($R\bar{3}$) were found to be consistent with the paths in Na_3MCl_6, as shown in Fig. 2, while the energy barrier between the migration paths was slightly decreased compared to Na_3MCl_6 (Fig. S5†). The Na-ion migration paths in Na_3GdI_6 for the $C2/m$ phase include three-dimensional paths between octahedral sites connected by tetrahedral interstitial sites (Oct.–Tet.–Oct.). Details of the migration paths in Na_3InBr_6 ($P\bar{3}1c$), Na_3ErBr_6 ($P2_1/n$), Na_3GdBr_6 ($R\bar{3}$) and Na_3GdI_6 ($C2/m$) are presented in Fig. S6–S9,† respectively.

The Na-ion migration energy barriers (E_a) in the $P\bar{3}1c$, $P2_1/n$ and $R\bar{3}$ phases of Na_3MX_6 (M = In, Er, Gd; X = Cl, Br) and the $C2/m$ phase of Na_3GdI_6 were predicted using BVSE, as shown in Fig. 2 and S5.† The trigonal $P\bar{3}1c$ and $R\bar{3}$ phases of Na_3MCl_6 exhibited E_a of 0.45 and 0.35 eV, respectively, for the 1D paths between face sharing octahedral sites (Na1–i1), and E_a of 0.53

24304 | *J. Mater. Chem. A*, 2022, **10**, 24301–24309

This journal is © The Royal Society of Chemistry 2022
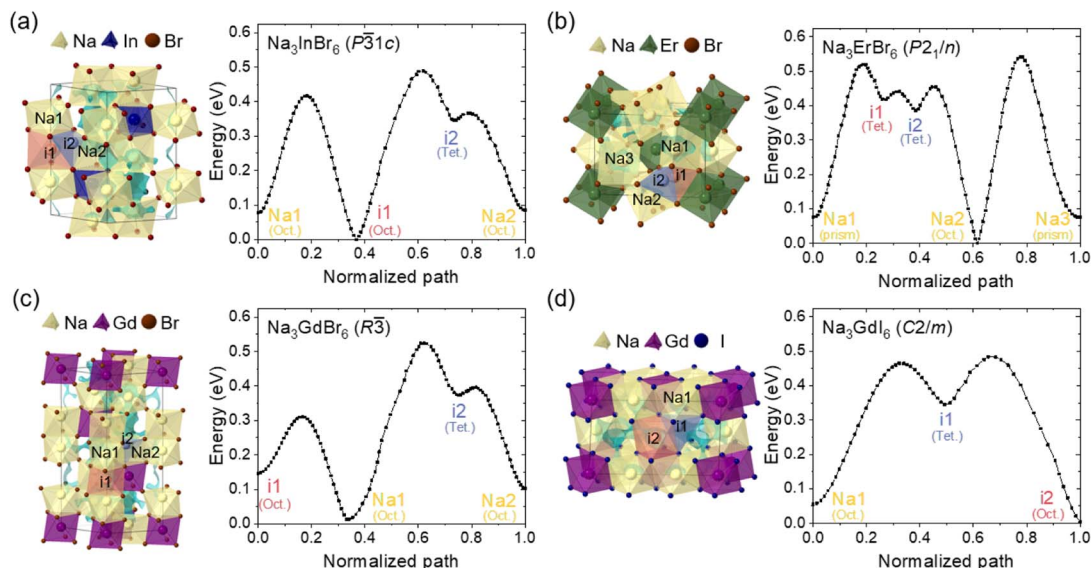
Fig. 2 Na-ion potential energy landscape of (a) Na_3InBr_6 (trigonal $P\bar{3}1c$), (b) Na_3ErBr_6 (monoclinic $P2_1/n$), (c) Na_3GdBr_6 (trigonal $R\bar{3}$) and (d) Na_3GdI_6 (monoclinic $C2/m$) calculated using the BVSE method, including Na-ion migration energy barriers along the migration paths. Details of migration paths are shown in Fig. S6–S9.†

and 0.65 eV, respectively, for the 3D paths between octahedral sites through the interstitial tetrahedral site (i1–i2–Na2 and Na1–i2–Na2). Note that E_a for the 3D paths is the key determiner for long-range migration rates. The E_a values in the $P2_1/n$ phase of Na_3MCl_6 were 0.60 eV for migration paths between octahedral and prism sites through tetrahedral interstitial sites (Na1–i1–i2–Na2) and 0.70 eV for the migration paths between octahedral and prism sites (Na2–Na3). The higher values of E_a for the $R\bar{3}$ and $P2_1/n$ phases indicate that the Na-ion diffusivity would be reduced for those phases. The $P\bar{3}1c$, $P2_1/n$ and $R\bar{3}$ phases of Na_3MBr_6 exhibited slightly lower E_a than those of Na_3MCl_6 as shown in Fig. 2. The E_a for the 3D paths in the $P\bar{3}1c$, $P2_1/n$ and $R\bar{3}$ phases of Na_3MBr_6 were 0.49, 0.54 and 0.52 eV, respectively, suggesting an improvement in Na-ion migration in Na_3MBr_6. The E_a value for the $C2/m$ phase of Na_3GdI_6 was computed as 0.48 eV for the 3D paths between octahedral sites through the interstitial tetrahedral sites (Na1–i1–i2), indicating that Na-ion diffusivity in the $C2/m$ phase would be higher than in other phases. The E_a value for the 1D and 3D paths of Na_3MX_6 (M = In, Er, Gd; X = Cl, Br) and Na_3GdI_6 are listed in Table S8.†

In addition to simple empirical BVSE calculations,[58,59] further detailed analysis of Na-ion migration in the $P\bar{3}1c$, $P2_1/n$ and $R\bar{3}$ phases of Na_3MX_6 (X = Br and I) were performed using AIMD simulations. The Na-ion diffusivity in Na_3InBr_6 ($P\bar{3}1c$), Na_3ErBr_6 ($P2_1/n$), Na_3GdBr_6 ($R\bar{3}$), Na_3YI_6 ($C2/m$) and Na_3GdI_6 ($C2/m$) were evaluated using the Na-ion mean squared displacement (MSD), as shown in Fig. S10.† Na_3ErBr_6 ($P2_1/n$) showed negligible Na-ion MSD over 100 ps at 900 K (Fig. S11†), suggesting the low ionic conductivity of Na_3MBr_6 with $P2_1/n$ structure. According to earlier studies, the ionic conductivity of Na_3ErBr_6 should be approximately 10^{-9} S cm^{-1}, reflecting the fact that inter-site hopping was not observed in the MSD plot at 900 K.[60] The Na-ion diffusivities of Na_3MBr_6 were improved in

the $P\bar{3}1c$ and $R\bar{3}$ phases, and $P\bar{3}1c$ showed the highest diffusivity among the $P\bar{3}1c$, $P2_1/n$ and $R\bar{3}$ phases of Na_3MBr_6. Note that, in Fig. 3(a), the Na-ion diffusivities of Na_3InBr_6 ($P\bar{3}1c$) at 900 and 1000 K (open triangles) are extrapolated values from the lower-temperature simulations because Na_3InBr_6 melted at high temperature.

As shown in Fig. 3(b), Na_3GdBr_6 ($R\bar{3}$) exhibited activation energy of 0.50 eV and ionic conductivity of 1.2×10^{-6} S cm^{-1} at room temperature. Na-ion MSD was found to further improve in Na_3InBr_6 ($P\bar{3}1c$), exhibiting activation energy of 0.37 eV and ionic conductivity of 5.8×10^{-5} S cm^{-1} at room temperature. The $C2/m$ phase of Na_3MI_6 showed lower activation energy and higher ionic conductivity compared with the $P\bar{3}1c$ and $R\bar{3}$ phases of Na_3MBr_6. Na_3GdI_6 and Na_3YI_6 exhibited activation energies of 0.30 and 0.34 eV and ionic conductivities of 5.9×10^{-4} and 2.4×10^{-4} S cm^{-1} at room temperature, respectively. The activation energies, ionic conductivities and error bounds are listed in Tables 1 and S9.† The activation energy and Na ionic conductivity of the $C2/m$ phase of Na_3YI_6 showed good agreement with previous theoretical work[39] reporting 0.32 eV and 3.5 $\times 10^{-4}$ S cm^{-1}, respectively. In the earlier study, the high ionic conductivity of $C2/m$ phase was predicted for Na_3YCl_6 and Na_3YBr_6,[38] but $P2_1/n$ phase was favorable structure for Na_3YCl_6, exhibiting low ionic conductivity approximately 10^{-9} S cm^{-1}.[35]

The isosurfaces of the Na-ion probability densities were plotted using an isosurface value of $2P_0$ for Na_3InBr_6 ($P\bar{3}1c$), Na_3GdBr_6 ($R\bar{3}$) and Na_3GdI_6 ($C2/m$) in Fig. 3(c–e), respectively, based on the Na-ion trajectories during 50 ps AIMD simulations at 800 K. As predicted from the relatively low values of E_a for the 1D paths in the $P\bar{3}1c$ and $R\bar{3}$ phases (Fig. 2), Na-ion isosurfaces were more connected for 1D paths along the z-axis, as shown in Fig. 3(c and d), S12 and S13.† The higher E_a for the 3D paths in $R\bar{3}$ phases inhibited long-range diffusion along the xy plane,
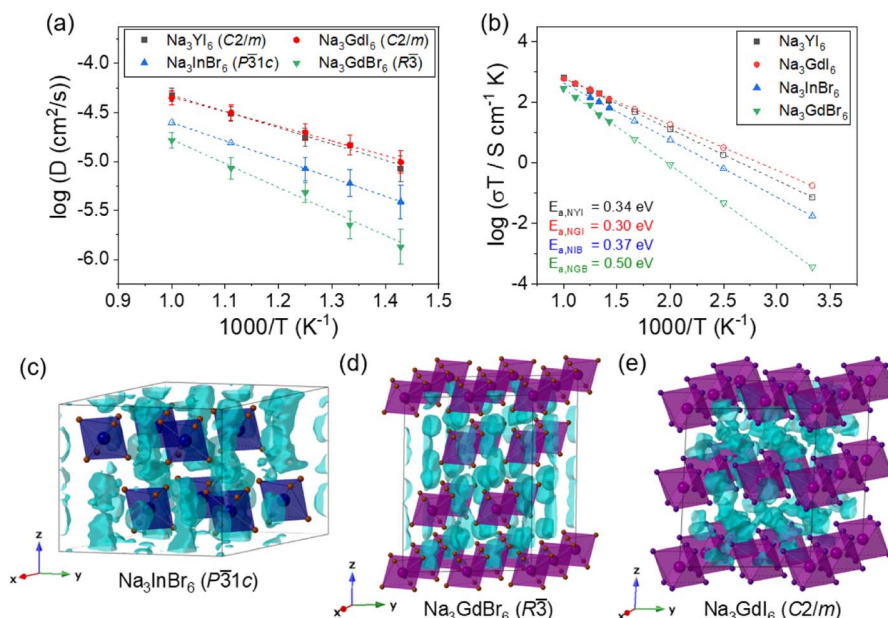
Fig. 3 Arrhenius plots of Na-ion (a) diffusivity and (b) conductivity for Na_3InBr_6, Na_3GdBr_6, Na_3YI_6 and Na_3GdI_6. The open symbols in (a) and (b) correspond to the ionic conductivities obtained by extrapolating from low- and high-temperature data, respectively. (c–e) Isosurfaces of the Na-ion probability densities (light blue) from 50 ps AIMD calculations at 800 K, plotted using an isosurface value of $2P_0$ for (c) Na_3InBr_6, (d) Na_3GdBr_6 and (e) Na_3GdI_6, where P_0 is mean ionic probability density. The octahedra in (c–e) correspond to $InBr_6$, $GdBr_6$ and GdI_6, respectively.

Table 1 Na ionic conductivities and activation energies of superionic Na halide SEs

Composition	Structure	σ at 300 K (mS cm^{-1})	E_a (eV)
Na_3InBr_6	$P\bar{3}1c$	0.058	0.37
Na_3ErBr_6	$P2_1/n$	10^{-6}	N/A
Na_3GdBr_6	$R\bar{3}$	0.0012	0.50
Na_3YI_6	$C2/m$	0.24	0.34
Na_3YI_6 (ref. 39)	$C2/m$	0.35	0.32
Na_3GdI_6	$C2/m$	0.59	0.30
$Na_3YBr_3I_3$	$C2/m$	3.3	0.25
$Na_3GdBr_3I_3$	$C2/m$	7.5	0.21

resulting in the low ionic conductivity of $R\bar{3}$. The Na-ion diffusivity increased in the $P\bar{3}1c$ phase for Na_3MBr_6 as diffusion along the 3D paths is facilitated in this phase, as shown in Fig. S12.† In Fig. 3(e) and S14,† it can be seen that the isosurfaces in Na_3GdI_6 are well connected through the 3D paths, verifying the high diffusivity in the $C2/m$ phase.

Anion mixing was performed to increase the ionic conductivity of the $C2/m$ phase Na_3MI_6, based on previous studies showing that Cl–Br mixing enhanced the ionic conductivity of Li_3MCl_6 owing to the increase in disorder in chemical bonding.[57,61,62] $Na_3MBr_xI_{6-x}$ (M = Y and Gd) structures with the lowest energy among 100 randomly generated simulation cells were used for the calculations. The phase stability of $Na_3MBr_xI_{6-x}$ was examined using the decomposition energy, E_d, as shown in Table S10.† $Na_3MBr_xI_{6-x}$ was found to be a metastable phase and it showed a phase transition from $C2/m$ to $R\bar{3}$ as the ratio of Br in $Na_3MBr_xI_{6-x}$ increased ($x > 3$).

The Na-ion diffusivity and conductivity of the $C2/m$ phase in $Na_3MBr_3I_3$ (M = Y and Gd) were evaluated using AIMD simulations, as shown in Fig. 4. The Arrhenius plot of the Na-ion diffusivity in Fig. 4(a) was obtained using the Na-ion MSD (Fig. S15†). $Na_3YBr_3I_3$ and $Na_3GdBr_3I_3$ exhibited activation energies of 0.25 and 0.21 eV and ionic conductivities of 3.3×10^{-3} and 7.5×10^{-3} S cm^{-1} at room temperature, respectively. Anion mixing with Br in the $C2/m$ phase of Na_3MI_6 was found to be a valuable strategy to enhance the ionic conductivity. The predicted ionic conductivity of $Na_3GdBr_3I_3$ (7.5 mS cm^{-1}) is the highest value among the studied Na halide SEs. The activation energies, ionic conductivities and error bounds for $Na_3YBr_3I_3$ and $Na_3GdBr_3I_3$ are listed in Tables 1 and S11.† The isosurfaces of the ionic probability densities for Na_3GdI_6 and $Na_3GdBr_3I_3$ are presented in Fig. 4(c) using an isosurface value of $2P_0$ based on the Na-ion trajectories from 50 ps AIMD simulations at 800 K. The ionic probability densities for Na, Br and I are shown in light blue, orange and blue, respectively. The isosurfaces of the Na-ion probability densities for $Na_3GdBr_3I_3$ were found to be more connected through the 3D paths than those for Na_3GdI_6, confirming the higher Na-ion diffusivity in $Na_3GdBr_3I_3$. Anion mixing likely increases disorder in the chemical bonding and enlarges the vibration of Br and I anions in the crystal lattice, which facilitates Na-ion migration. The isosurfaces of the ionic probability densities with views along various directions are shown in Fig. S16 and S17.†

The electrochemical stability window of Na_3MX_6 (X = Cl, Br and I) was evaluated using a grand potential diagram as a function of the chemical potential of Na. As shown in Fig. 5, Na_3MCl_6 and Na_3MBr_6 display high oxidation potential of approximately 3.9 and 3.7 V, respectively, suggesting good
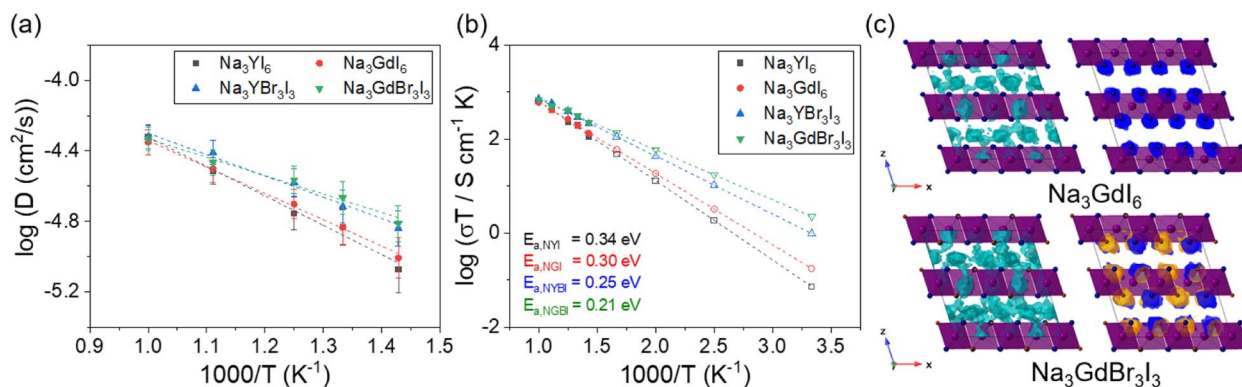
24306 | *J. Mater. Chem. A*, 2022, **10**, 24301–24309

This journal is © The Royal Society of Chemistry 2022

Fig. 4 Arrhenius plots of Na-ion (a) diffusivity and (b) conductivity for Na_3YI_6, Na_3GdI_6, $Na_3YBr_3I_3$ and $Na_3GdBr_3I_3$. The open symbols in (b) correspond to the ionic conductivities obtained by extrapolating from high-temperature data. (c) Isosurfaces of the ionic probability densities for Na, Br and I (light blue, orange and blue, respectively) from 50 ps AIMD calculations at 800 K, plotted using an isosurface value of $2P_0$ for Na_3GdI_6 and $Na_3GdBr_3I_3$. The octahedra in (c) correspond to $GdBr_xI_{6-x}$.
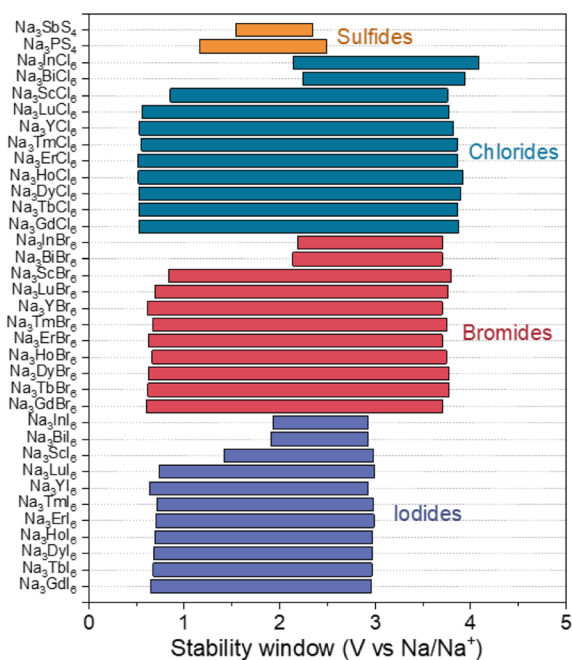

Fig. 5 Electrochemical stability windows of Na halide (Na_3MX_6, X = Cl, Br and I) and sulfide (Na_3PS_4 and Na_3SbS_4) SEs.

reaction. Interface coatings could be applied to passivate the oxidative decomposition of Na_3MI_6.[33]

The reduction potentials of Na_3MX_6 (X = Cl, Br and I) were found to depend on the identity of the M element, agreeing with previous studies on Li halides Li_3MX_6 that electronegativity difference between M and X affected electrochemical stabilities.[57] Stronger electron localization between M and X would decrease the reduction potential. The reduction potentials of Na_3MX_6 with p-block elements are approximately 2.1 V, whereas Na_3MX_6 with group 3 elements and lanthanides exhibit a much lower reduction potential of approximately 0.6 V. Overall, however, the Na_3MX_6 compounds generally show a wide electrochemical window. Reductive decomposition resulted in the formation of metallic compounds, as shown in Table S12,† enabling continuous reduction reactions of Na_3MX_6 by conducting electrons.[64] Therefore, we suggest that interfacial coatings between the Na metal anode and Na_3MX_6 would be required to inhibit the continuous reductive decomposition of Na_3MX. The oxidation and reduction potentials of Na_3MX_6 and the phase equilibria at these potentials are summarized in Table S12.†

electrochemical stability against oxidation at high voltages. We point out that, under real conditions, oxidation reactions typically occur at potentials higher than these theoretical limits owing to the kinetic barrier for the phase decomposition reaction and the presence of protective decomposition layers at the interface. Therefore, Na_3MCl_6 and Na_3MBr_6 could be applied to ASSBs with high-voltage cathodes and they show substantial advantages compared with sulfide SEs with low oxidation potentials (<2.5 V), such as Na_3PS_4 and Na_3SbS_4.[63] Na_3MI_6 exhibits an oxidation potential of approximately 3.0 V, suggesting lower electrochemical stability against oxidation than Na_3MCl_6 and Na_3MBr_6. Again, kinetic reaction barriers and decomposition layers may help to prevent the oxidation

Conclusions

In this study, we have provided design principles of superionic Na halide SEs through systematic analyses of the structural preference, phase stability, electrochemical stability and transport properties of Na_3MX_6 (X = Cl, Br and I). The structures of Na_3MX_6 are strongly dependent on the types and sizes of cations M and anions X, and the octahedral factors were found to be effective descriptors for predicting the stable phases of Na_3MX_6. Na_3MX_6 generally exhibits $P\bar{3}1c$, $P2_1/n$, $R\bar{3}$ and $C2/m$ phases, while Na_3MX_6 with relatively small M cations exhibits the $NaMX_4$ ($P2_12_12_1$) phase. Na_3MCl_6 and Na_3MBr_6 prefer the $P\bar{3}1c$, $P2_1/n$ and $R\bar{3}$ phases and phase transitions from $P\bar{3}1c$–$P2_1/n$–$R\bar{3}$ were found to occur with increasing size of M. Na_3MI_6 showed octahedral factor values similar to those of the $C2/m$ phase of Li_3MCl_6, indicating a preference for the $C2/m$ phase

This journal is © The Royal Society of Chemistry 2022

J. Mater. Chem. A, 2022, **10**, 24301–24309 | **24307**

over the $P\bar{3}1c$, $P2_1/n$ and $R\bar{3}$ phases. The effects of the structures of Na_3MX_6 on Na-ion migration were investigated using the BVSE method and AIMD simulations. The energy barriers of Na-ion migration in the $R\bar{3}$ and $P2_1/n$ phases were found to be higher than those in the $P\bar{3}1c$ phase for Na_3MCl_6 and Na_3MBr_6, whereas the $C2/m$ phase Na_3MI_6 showed a lower barrier than the other phases. AIMD simulations likewise revealed that the $P\bar{3}1c$ phase exhibits high ionic conductivity ($\sim10^{-5}$ S cm^{-1}) relative to the other phases of Na_3MBr_6 and that the $C2/m$ phase of Na_3MI_6 shows even higher ionic conductivity ($\sim10^{-4}$ S cm^{-1}). Anion mixing with Br in Na_3MI_6 further enhanced Na-ion migration, resulting in a superb ionic conductivity of 7.5×10^{-3} S cm^{-1} for $Na_3GdBr_3I_3$, which is the highest value among the reported Na halide SEs. Na_3MCl_6 and Na_3MBr_6 exhibit natively high oxidation potentials, enabling compatibility with high-voltage cathodes (~4 V), whereas interfacial coatings would be required to use Na_3MI_6 with high-voltage cathodes. The material design principles in this work provide fundamental guidelines for the development of superionic Na halide SEs for high-voltage Na ASSBs.

Conflicts of interest

There are no conflicts to declare.

Acknowledgements

References

1 D. Larcher and J. M. Tarascon, *Nat. Chem.*, 2015, **7**, 19–29.
2 A. Manthiram, X. Yu and S. Wang, *Nat. Rev. Mater.*, 2017, **2**, 16103.
3 S. Randau, D. A. Weber, O. Kötz, R. Koerver, P. Braun, A. Weber, E. Ivers-Tiffée, T. Adermann, J. Kulisch, W. G. Zeier, F. H. Richter and J. Janek, *Nat. Energy*, 2020, **5**, 259–270.
4 J. B. Goodenough and Y. Kim, *Chem. Mater.*, 2010, **22**, 587–603.
5 P. Albertus, S. Babinec, S. Litzelman and A. Newman, *Nat. Energy*, 2018, **3**, 16–21.
6 M. Cheng, Y. Wang, D. Zhang, S. Zhang, Y. Yang, X. Lv, J. Wang and Y. NuLi, *J. Energy Chem.*, 2023, **76**, 1–10.
7 S. Trano, F. Corsini, G. Pascuzzi, E. Giove, L. Fagiolari, J. Amici, C. Francia, S. Turri, S. Bodoardo, G. Griffini and F. Bella, *ChemSusChem*, 2022, **15**, e202200294.
8 F. Bella, S. De Luca, L. Fagiolari, D. Versaci, J. Amici, C. Francia and S. Bodoardo, *Nanomaterials*, 2021, **11**, 810.
9 M. Song, Y. Wang, B. Yu, W. Yang, G. Cheng, W. Cui and Z. Zhang, *Chem. Eng. J.*, 2022, **450**, 138176.
10 E. Manarin, F. Corsini, S. Trano, L. Fagiolari, J. Amici, C. Francia, S. Bodoardo, S. Turri, F. Bella and G. Griffini, *ACS Appl. Polym. Mater.*, 2022, **4**, 3855–3865.
11 A. Massaro, A. B. Muñoz-García, P. Maddalena, F. Bella, G. Meligrana, C. Gerbaldi and M. Pavone, *Nanoscale Adv.*, 2020, **2**, 2745–2751.
12 W. Hou, X. Guo, X. Shen, K. Amine, H. Yu and J. Lu, *Nano Energy*, 2018, **52**, 279–291.
13 Y. Lu, L. Li, Q. Zhang, Z. Niu and J. Chen, *Joule*, 2018, **2**, 1747–1770.
14 C. Zhao, L. Liu, X. Qi, Y. Lu, F. Wu, J. Zhao, Y. Yu, Y.-S. Hu and L. Chen, *Adv. Energy Mater.*, 2018, **8**, 1703012.
15 Y. Wang, S. Song, C. Xu, N. Hu, J. Molenda and L. Lu, *Nano Mater. Sci.*, 2019, **1**, 91–100.
16 T. Krauskopf, C. Pompe, M. A. Kraft and W. G. Zeier, *Chem. Mater.*, 2017, **29**, 8859–8869.
17 A. Banerjee, K. H. Park, J. W. Heo, Y. J. Nam, C. K. Moon, S. M. Oh, S.-T. Hong and Y. S. Jung, *Angew. Chem., Int. Ed.*, 2016, **55**, 9634–9638.
18 A. Hayashi, N. Masuzawa, S. Yubuchi, F. Tsuji, C. Hotehama, A. Sakuda and M. Tatsumisago, *Nat. Commun.*, 2019, **10**, 5266.
19 Z. Zhang, E. Ramos, F. Lalère, A. Assoud, K. Kaup, P. Hartman and L. F. Nazar, *Energy Environ. Sci.*, 2018, **11**, 87–93.
20 T. Fuchs, S. P. Culver, P. Till and W. G. Zeier, *ACS Energy Lett.*, 2020, **5**, 146–151.
21 Y. Xiao, Y. Wang, S.-H. Bo, J. C. Kim, L. J. Miara and G. Ceder, *Nat. Rev. Mater.*, 2020, **5**, 105–126.
22 Y. Lee, J. Jeong, H. J. Lee, M. Kim, D. Han, H. Kim, J. M. Yuk, K.-W. Nam, K. Y. Chung, H.-G. Jung and S. Yu, *ACS Energy Lett.*, 2022, **7**, 171–179.
23 N. Anantharamulu, K. Koteswara Rao, G. Rambabu, B. Vijaya Kumar, V. Radha and M. Vithal, *J. Mater. Sci.*, 2011, **46**, 2821–2837.
24 M.-C. Bay, M. Wang, R. Grissa, M. V. F. Heinz, J. Sakamoto and C. Battaglia, *Adv. Energy Mater.*, 2020, **10**, 1902899.
25 J. Liang, X. Li, K. R. Adair and X. Sun, *Acc. Chem. Res.*, 2021, **54**, 1023–1033.
26 X. Li, J. Liang, X. Yang, K. R. Adair, C. Wang, F. Zhao and X. Sun, *Energy Environ. Sci.*, 2020, **13**, 1429–1461.
27 S. Wang, Q. Bai, A. M. Nolan, Y. Liu, S. Gong, Q. Sun and Y. Mo, *Angew. Chem., Int. Ed.*, 2019, **58**, 8039–8043.
28 H. Kwak, S. Wang, J. Park, Y. Liu, K. T. Kim, Y. Choi, Y. Mo and Y. S. Jung, *ACS Energy Lett.*, 2022, **7**, 1776–1805.
29 T. Asano, A. Sakai, S. Ouchi, M. Sakaida, A. Miyazaki and S. Hasegawa, *Adv. Mater.*, 2018, **30**, 1803075.
30 X. Li, J. Liang, J. Luo, M. Norouzi Banis, C. Wang, W. Li, S. Deng, C. Yu, F. Zhao, Y. Hu, T.-K. Sham, L. Zhang, S. Zhao, S. Lu, H. Huang, R. Li, K. R. Adair and X. Sun, *Energy Environ. Sci.*, 2019, **12**, 2665–2671.

24308 | *J. Mater. Chem. A*, 2022, **10**, 24301–24309

This journal is © The Royal Society of Chemistry 2022

31 J. Liang, X. Li, S. Wang, K. R. Adair, W. Li, Y. Zhao, C. Wang, Y. Hu, L. Zhang, S. Zhao, S. Lu, H. Huang, R. Li, Y. Mo and X. Sun, *J. Am. Chem. Soc.*, 2020, **142**, 7012–7022.

32 L. Zhou, T.-T. Zuo, C. Y. Kwok, S. Y. Kim, A. Assoud, Q. Zhang, J. Janek and L. F. Nazar, *Nat. Energy*, 2022, **7**, 83–93.

33 S. Yu, H. Park and D. J. Siegel, *ACS Appl. Mater. Interfaces*, 2019, **11**, 36607–36615.

34 R. Schlem, A. Banik, M. Eckardt, M. Zobel and W. G. Zeier, *ACS Appl. Energy Mater.*, 2020, **3**, 10164–10173.

35 E. A. Wu, S. Banerjee, H. Tang, P. M. Richardson, J.-M. Doux, J. Qi, Z. Zhu, A. Grenier, Y. Li, E. Zhao, G. Deysher, E. Sebti, H. Nguyen, R. Stephens, G. Verbist, K. W. Chapman, R. J. Clément, A. Banerjee, Y. S. Meng and S. P. Ong, *Nat. Commun.*, 2021, **12**, 1256.

36 H. Kwak, J. Lyoo, J. Park, Y. Han, R. Asakura, A. Remhof, C. Battaglia, H. Kim, S.-T. Hong and Y. S. Jung, *Energy Storage Mater.*, 2021, **37**, 47–54.

37 D. Park, K. Kim, G. H. Chun, B. C. Wood, J. H. Shim and S. Yu, *J. Mater. Chem. A*, 2021, **9**, 23037–23045.

38 Y. Qie, S. Wang, S. Fu, H. Xie, Q. Sun and P. Jena, *J. Phys. Chem. Lett.*, 2020, **11**, 3376–3383.

39 H. Huang, H.-H. Wu, C. Chi, Y. Yang, J. Zheng, B. Huang and S. Wang, *J. Mater. Chem. A*, 2021, **9**, 26256–26265.

40 A. Bohnsack and G. Meyer, *Z. Anorg. Allg. Chem.*, 1997, **623**, 837–843.

41 G. Mairesse, P. Barbier and J.-P. Wignacourt, *Acta Crystallogr., Sect. B: Struct. Crystallogr. Cryst. Chem.*, 1979, **35**, 1573–1580.

42 T. Staffel and G. Meyer, *Z. Anorg. Allg. Chem.*, 1989, **574**, 107–113.

43 G. Kresse and J. Furthmüller, *Phys. Rev. B: Condens. Matter Mater. Phys.*, 1996, **54**, 11169–11186.

44 G. Kresse and D. Joubert, *Phys. Rev. B: Condens. Matter Mater. Phys.*, 1999, **59**, 1758–1775.

45 P. E. Blöchl, *Phys. Rev. B: Condens. Matter Mater. Phys.*, 1994, **50**, 17953–17979.

46 J. P. Perdew, K. Burke and M. Ernzerhof, *Phys. Rev. Lett.*, 1996, **77**, 3865–3868.

47 J. Klimeš, D. R. Bowler and A. Michaelides, *J. Phys.: Condens. Matter*, 2009, **22**, 022201.

48 S. P. Ong, W. D. Richards, A. Jain, G. Hautier, M. Kocher, S. Cholia, D. Gunter, V. L. Chevrier, K. A. Persson and G. Ceder, *Comput. Mater. Sci.*, 2013, **68**, 314–319.

49 G. Friedrich, H. Fink and H. J. Seifert, *Z. Anorg. Allg. Chem.*, 1987, **548**, 141–150.

50 M. Beran and G. Meyer, *Crystals*, 2011, **1**, 99–103.

51 G. Meyer, *Z. Anorg. Allg. Chem.*, 1984, **517**, 191–197.

52 H. Chen, L. L. Wong and S. Adams, *Acta Crystallogr., Sect. B: Struct. Crystallogr. Cryst. Chem.*, 2019, **75**, 18–33.

53 X. He, Y. Zhu, A. Epstein and Y. Mo, *npj Comput. Mater.*, 2018, **4**, 18.

54 Y. Liu, S. Wang, A. M. Nolan, C. Ling and Y. Mo, *Adv. Energy Mater.*, 2020, **10**, 2002356.

55 A. Jain, S. P. Ong, G. Hautier, W. Chen, W. D. Richards, S. Dacek, S. Cholia, D. Gunter, D. Skinner, G. Ceder and K. A. Persson, *APL Mater.*, 2013, **1**, 011002.

56 Y. Yu, Z. Wang and G. Shao, *J. Mater. Chem. A*, 2021, **9**, 25585–25594.

57 K. Kim, D. Park, H.-G. Jung, K. Y. Chung, J. H. Shim, B. C. Wood and S. Yu, *Chem. Mater.*, 2021, **33**, 3669–3677.

58 R. Xiao, H. Li and L. Chen, *Sci. Rep.*, 2015, **5**, 14227.

59 D. Park, H. Park, Y. Lee, S.-O. Kim, H.-G. Jung, K. Y. Chung, J. H. Shim and S. Yu, *ACS Appl. Mater. Interfaces*, 2020, **12**, 34806–34814.

60 A. D. Sendek, E. D. Cubuk, E. R. Antoniuk, G. Cheon, Y. Cui and E. J. Reed, *Chem. Mater.*, 2019, **31**, 342–352.

61 Z. Liu, S. Ma, J. Liu, S. Xiong, Y. Ma and H. Chen, *ACS Energy Lett.*, 2021, **6**, 298–304.

62 A. Zevgolis, B. C. Wood, Z. Mehmedović, A. T. Hall, T. C. Alves and N. Adelstein, *APL Mater.*, 2018, **6**, 047903.

63 H. Tang, Z. Deng, Z. Lin, Z. Wang, I.-H. Chu, C. Chen, Z. Zhu, C. Zheng and S. P. Ong, *Chem. Mater.*, 2018, **30**, 163–173.

64 L. M. Riegger, R. Schlem, J. Sann, W. G. Zeier and J. Janek, *Angew. Chem., Int. Ed.*, 2021, **60**, 6718–6723.

This journal is © The Royal Society of Chemistry 2022

J. Mater. Chem. A, 2022, **10**, 24301–24309 | **24309**